# Effect of Fe Substitution for Cu on Microstructure and Magnetic Properties of Laser Floating Zone (LFZ) Grown Bi-2212 Rods

M. Ozabaci[1], A. Sotelo[2], M.A. Madre[2], M.E. Yakinci[1]

[1]SEM/EDX Laboratuvarı, Bilimsel ve Teknolojik Arasturma Merkezi (IBTAM), Inönü Üniversitesi, 44280, Malatya, Turkey

[2]Instituto de Ciencia de Materiales de Aragón (ICMA), CSIC-Universidad de Zaragoza, Maria de Luna, 3, 50018, Zaragoza, Spain

## Abstract

In this paper, the laser floating zone (LFZ) technique has been used to fabricate $Bi_2Sr_2Ca_1Cu_{2-x}Fe_xO_8$ ($x$ = 0, 0.01, 0.03, 0.05, 0.1) superconducting fibers. The effect of Fe substitution on grain alignment and superconducting properties of annealed fibers were studied using SEM/EDX microanalysis in addition to phase analysis and magnetic measurements realized through XRD, $M$–$T$ , and $M$–$H$ loops. In the same growth conditions, higher Fe contents lead to a more compact microstructure with lower porosity but also caused the formation of poor superconducting phases followed by the decrease of $T_c$ and $J_{cmag}$. No evidence of enhanced pinning capability was found in the magnetic measurements. Annealed rods indicated a weakly ferromagnetic-like behavior at relatively high doping levels.

**Keywords:** Bi-2212; Fe substitution; LFZ; Texture; Melt processing

Corresponding Author:

M. Ozabaci. SEM/EDX Laboratuvarı, Bilimsel ve Teknolojik Arasturma Merkezi (IBTAM), Inönü Üniversitesi, 44280, Malatya, Turkey. muratozabaci@yahoo.com.

## 1 Introduction

Just after the discovery of superconductivity in copper-based oxides, great efforts have been made in order to find the basic parameters which are responsible for the superconducting properties of these compounds [1,2]. Among high-$T_c$ superconducting (HTS) systems, Bi-based cuprates deserved special attention owing to their promising chemical stability, absence of rare earths, relatively high critical temperature and, when properly processed, high critical current density. From the point of view of technological applications, preparation techniques of superconducting materials are so important as the material type. When the current-carrying capacity of the material is regarded, it is seen that the major limitations come from intergrain weak links and weak flux pinning capabilities for the superconducting materials. Oriented grains together with artificially doped structures have been considered to be effective solutions to overcome these limitations. Within this scope many different techniques have been developed so far to obtain materials with highly aligned grains [3–6]. Of all these techniques, the Laser Floating Zone (LFZ) technique has been shown to be an outstanding technique in terms of grain alignment, reproducibility, speed, and cost. This technique has been successfully applied so far for the high-$T_c$ superconductors, especially for the Bi-2212 phase, as well as on similarly layered materials such the thermoelectric oxidic ceramics [7–10]. Materials produced by this technique are nearly free of low angle grain boundaries, allowing $J_{c\text{-trans}}$ values as high as 5500 A/cm$^2$ at 77 K [11,12].

In order to increase the impact of this technique in the superconducting materials processing and use it in the most effective way, the influence of several fundamental parameters like pulling and feeding speeds, laser type and power, growing atmosphere, rotation rates between feed and seed rods, as well as precursor powder stoichiometry on the alignment and homogeneity of as-grown fibers were investigated deeply in different studies so far [13,14]. Although large numbers of studies have been devoted to improve the LFZ growth parameters, doping in the LFZ grown superconducting fibers has attracted less interest [15].

In this study, structural and magnetic properties of LFZ grown $Bi_2Sr_2CaCu_{2-x}Fe_xO_8$ ($x$ = 0, 0.01, 0.03, 0.05, 0.1) fibers were investigated. Iron substitutions have been made instead of copper by taking into account some theoretical models asserting that Cu atoms in the Cu–O plane play a crucial role in the superconductivity mechanism [16]. The aim of this work is the improvement of critical current density by producing effective flux pinning centers in the structure as a result of Fe addition.

## 2 Experimental

$Bi_2Sr_2CaCu_{2-x}Fe_xO_8$ ($x$ = 0, 0.01, 0.03, 0.05, 0.1) powders were synthesized by the classical solid state route. In this method, doped-BSCCO bars, have been prepared from commercial $Bi_2O_3$ (Panreac, 98+ %), $SrCO_3$ (Panreac, 98+ %), $CaCO_3$ (Panreac, 98.5+ %), CuO (Panreac, 97+ %) and $Fe_2O_3$ (Panreac, 96 %) powders. The weighed powders in adequate atomic proportions were ball-milled using agate balls and acetone for 30 minutes at 300 rpm to obtain a homogeneous mixture. The resulting suspension was dried using IR radiation in order to evaporate the maximum amount of acetone. The resulting mixture was placed in a furnace and heated slowly to 750 ºC, where it was kept for ca. 12 h, followed by furnace cooling. After cooling, the remaining powder was manually ground and heated again at 800 ºC for 12 h, milled and isostatically pressed at ca. 200 MPa in form of cylinders (1.5–3 mm diameter and 120 mm long).

The obtained cylinders were subsequently used as feed in a directional solidification process performed in a LFZ installation described elsewhere in detail [17]. The textured bars were obtained using a continuous power Nd:YAG laser ($\lambda$ = 1064 nm), under air, at a growth rate of 30 mm/h and a relative rotation of 18 rpm between seed and feed. As Bi-2212 compounds melt incongruently, after laser processing, the rods need a final thermal treatment to produce the Bi-2212 phase as the major one. This annealing process consisted of two steps: 60 h at 860 ºC, followed by 12 h at 800 ºC and, finally, quenched in air to room temperature.

Phase analysis of all samples was performed by powder XRD utilizing a Rigaku RadB X-ray powder diffractometer (CuK$\alpha$ radiation) with 2$\theta$ ranging between 5 and

65 degrees at a scan rate of 3 º/min. Microstructural and elemental analysis of the fibers, both as-grown and annealed, were studied on polished longitudinal cross-sections by using LEO EVO-40XVP scanning electron microscope (SEM) equipped with a Bruker energy dispersive X-ray spectroscope (EDX) having a sensitivity up to 125 eV.

Magnetic measurements were performed in a Quantum Design PPMS (9 T) for fields applied parallel and perpendicularly to the growth axis. The magnetic hysteresis cycles were performed at different temperatures (5, 15, 25 K) and the magnetic critical current density was then estimated using Bean's model. $T_c$ values were determined from dc magnetization measurements of samples.

## 3 Results and Discussion

Figure 1 shows powder XRD patterns of pure and Fe-doped annealed rods for all doping range. Since the amount of iron substitution is not very large, the peaks originated by iron could not be detected in the spectrum. It was found that major peaks correspond to the Bi-2212 phase in all cases. For low doping rates, secondary phase formation is negligible. When the doping level reached the $x$ = 0.1, slight amounts of Ca-free and Bi-free secondary phases like 2201 and $Ca_3Cu_7O_{10}$, respectively, can be observed in the XRD spectra. So, the introduction of iron in the structure can act as an obstacle in the formation of Bi-2212 phase, promoting the formation of secondary phases. On the other hand, from these data it is not possible to confirm the Fe–Cu substitution in the crystal structure.

The relative higher intensity of (00l) diffraction peaks in XRD diagram is an important clue indicating the preferential orientation of grains along *c*-axis. The ratio of intensity of major (00*l*)/(*hkl*) (where *h, k*#0) peaks do not change for different doping levels, suggesting that substitution of Fe up to $x$ = 0.1 does not affect the grains orientation.

SEM/EDX microstructural studies on as-grown materials showed that all the textured rods with various doping levels have some common phases together with some small differences in elemental ratios depending on iron content. The main common two phases for the whole doping range are Bi-free $(Ca_{1-x}Sr_x)CuO_2$ and Bi-

rich intergrowths of 2212 and 2201 phases, which correspond to the dark gray and light gray contrasts, respectively, in BSE images, as shown in Fig. 2a–b. In addition to these two main phases minor amounts of unreacted metallic oxides with various geometries in black and dark gray contrast were found in EDX analysis. When the doping level reached the $x$ = 0.05, a new Sr and Fe-rich 2201 and 2212 intergrowth phase in middle gray contrast has been identified in the structure. Instead of agglomeration in some local points, Fe atoms successfully incorporated into the crystal structure of this new phase while it could not be detected in Bi-free secondary phase, $(Ca_{1-x}Sr_x)CuO_2$, as evidenced by dot mapping analysis shown in Figs. 2 and 3d. It can be concluded from Fig. 2a–b increasing doping ratio, surprisingly, lead to more uniform morphology with smaller grain dimensions and less porosity for the as-grown rods. This effect can be due to the raise in melt viscosity with metallic doping, leading to better uniformity on surface morphology. In spite of highly aligned grain structure, non-superconducting electrical properties of these rods have been attributed to heterogeneous phase structure deprived of long range phase coherence. Probably, because of insufficient time for the homogenization of molten zone and adjustment of oxygen stoichiometry in the growth process, material has not been able to reach a stable 2212 stoichiometry for the as-grown samples.

Thermal annealing produces the formation of Bi-2212 phase from the secondary phases, such as $(Ca_{1-x}Sr_x)CuO_2$, metallic oxides and 2201. It has been considered that during this conversion 2212 particles which has been already formed in the laser processing act as nucleation centers for further expansion of this high-$T_c$ phase [18]. SEM/EDX investigations of these annealed rods indicated that annealing produces the Bi-2212 phase as the major one in the inner part of the rods while for the outer part there still exist some Bi-free and CaO phases in relatively high amounts. There is still a probability to find all these phases in the annealed rods, but the main difference is related to the concentration and distribution of these phases. For example, Bi rich intergrowths of 2212 and 2201 still exist in the core but they can be found only in higher magnification SEM images. Similarly, Sr-rich 2212 and 2201 intergrowths, with high iron content, still

exist in the core but in lower amounts. Dot mapping images in Fig. 3d clearly indicate that unlike the image in Fig. 2d, Ca distribution on the surface is more homogeneous with the effect of thermal annealing.

The magnetic hysteresis cycles (*M–H*) of the annealed rods were obtained in the applied field range of ±9 Tesla at three different temperatures, 5, 15, and 25 K, Fig. 4. Magnetic field was applied both parallel and perpendicular to the rods growth axis. For the perpendicular case, a characteristic of $HT_c$ superconductors, symmetric *M–H* loops were obtained for the $x$ = 0.01 and 0.03 doping values, while for the parallel applied field perfect symmetrical behavior could only be obtained for the lowest doping amount, $x$ = 0.01. For higher Fe contents, all hysteresis loops displayed a weak ferromagnetic-like behavior due to the presence of Fe, indicating that iron electrons do not lose their ferromagnetic ordering after their incorporation to the Sr-rich 2212 lattice.

Diamagnetic properties of the rods indicate they are more resistive when the external field is applied parallel to the rods axis than in the perpendicular direction. On the contrary, the magnetization values are higher when the field was applied perpendicular to the growth axis. These effects are the consequence of the shielding currents paths, which generate the opposite field to provide zero net flux within the rods. For the perpendicular applied field, big portion of these currents flows through the growth axis with small deviations depending on the sample geometry. For the parallel applied field, it has been assumed that nearly all current flows perpendicular to the growth axis. Therefore, approximately 2–3 times larger widths of loops for the perpendicular case with respect to parallel applied field are another indication of the alignment of the grains with respect to the growth axis. When the influence of doping ratios on magnetization is regarded, it has been seen that weakening effect of iron doping on magnetic properties of the rods felt more in the perpendicular orientation than the parallel one. This could be explained with the worsening effect of doping on grain alignment with the growth axis.

Similarly, critical current densities of the rods, $J_{cmag}$, calculated by using Bean's critical state model, with the formula $J_{cmag} = 30.\ \Delta M/d$, gave the same anisotropy for the fields applied from the two different directions [19]. In this formula, $\Delta M$ is the

width of the magnetization loop at the applied magnetic field and *d* is the diameter of the cylindrical sample, assuming supercurrents flow within the entire sample. As seen in Fig. 5, the $J_{cmag}$ *(T)* curves follow an exponential *T* dependence over the whole temperature range. For the pure sample, $J_{\perp cmag}$ was found to be $3\times10^5$ A/cm$^2$ at 5 K for the zero applied field while for the $x$ = 0.1 doped one in the same conditions it is reduced until $9.5 \times 10^4$ A/cm$^2$. For the parallel applied field, these values were calculated to be $1.7 \times 10^5$ and $3.3 \times 10^4$ A/cm$^2$, respectively. For the whole doping range, increasing doping rates together with temperature always caused suppression on the width of *M–H* loops followed by a decrease in magnetic critical current values. This shows that increasing the amount of iron, the superconducting fraction within the material is reduced. It has been evaluated that flux pinning centers which were aimed to be obtained in the material in the scope of this study by substituting iron could not be obtained as evidenced by magnetic measurements in addition to EDX analysis which shows the penetration into and homogeneous distribution of iron the Sr-rich 2212 phase. In addition, although there is a more uniform structure, smaller size of grains, together with formation of minor amount of secondary phases (see Fig. 1), produces a degradation on the magnetic and electrical properties of these superconducting rods with increasing substitution level.

Transition temperatures ($T_c$-onset) of annealed rods were derived from dc magnetization versus temperature measurements which have been realized under applied field of 50 Oe, Fig. 6. Since these $T_c$-onset values are also a result of the rods' diamagnetic properties, the comments related with the deterioration effect of doping which have been made above regarding critical currents are also valid for the transition temperature values. At the highest doping level, $T_c$-onset reduces from 91.5 K to the 79.9 K for the field applied from perpendicular direction and for the parallel case these values are 90.7 K for the pure-2212 and 74.6 K for the $x$ = 0.1 as presented in Table 1.

## 4 Conclusions

Textured bulk materials with composition $Bi_2Sr_2CaCu_{2-x}Fe_xO_{8+\delta}$ ($x$ = 0, 0.01, 0.03, 0.05, 0.1) were successfully grown using the LFZ technique. It was shown that substitution of Fe degraded the superconducting properties of fibers by means of magnetic measurements. Against the increased uniformity and less porosity on microstructure with increasing doping ratio, formation of a new Sr-rich, Ca-poor 2212 phase together with some minor amount of secondary phases, for $x \geq 0.05$ Fe content, are considered to be the main detrimental factors. It was also found that iron doping with LFZ technique did not improve pinning properties of the rods.

**Acknowledgements**

This work was supported by the Scientific and Technological Research Council of Turkey (TUBITAK) in the scope of 2214 International Doctoral Research Fellowship Program. A. Sotelo and M.A. Madre acknowledge MICINN-FEDER (Project MAT2008-00429) and DGA (Consolidated research group T12) for financial support.

**References**

1. Maeda, H., Tanaka, Y., Fukutomi, M., Asano, T.: Jpn. J. Appl. Phys. **27**, L209 (1988)

2. Bednorz, J.G., Müller, K.A.: Z. Phys. B **64**, 188 (1986)

3. Cecchetti, E., Ferreira, P.J., Vander Sande, J.B.: Supercond. Sci. Technol. **13**, 1270 (2000)

4. Yoo, J.M., Mukherjee, K.: J. Mater. Sci. **29**, 4306 (1994)

5. Damborsky, K., Lu, F.,McIntyre, P., Pogue, N.: IEEE Trans. Appl. Supercond. **21**, 2783 (2011)

6. Garnier, V., Caillard, R., Sotelo, A., Desgardin, G.: Physica C **319**, 197 (1999)

7. Feigelson, R.S., Gazit, D., Fork, D.K., Geballe, T.H.: Science **240**, 1642 (1988)

8. Madre, M.A., Amaveda, H., Mora, M., Sotelo, A., Angurel, L.A., Diez, J.C.: Bol. Soc. Esp. Ceram. **47**, 148 (2008)

9. Costa, F.M., Carrasco, M.F., Ferrreira, N., Silva, R.F., Vieira, J.M.: Physica C **408–410**, 915 (2004)

10. Sotelo, A., Guilmeau, E., Madre, M.A., Marinel, S., Diez, J.C., Prevel, M.: J. Eur. Ceram. Soc. **27**, 3697 (2007)
11. Angurel, L.A., Diez, J.C., Martinez, E., Pena, J.I., de la Fuente, G.F., Navarro, R.: Physica C **302**, 39 (1998)
12. de la Fuente, G., Diez, J.C., Angurel, L.A., Pena, J.I., Sotelo, A., Navarro, R.: Adv. Mater. **7**, 853 (1995)
13. Sotelo, A., Rasekh, S., Madre, M.A., Diez, J.C.: J. Supercond. Nov. Magn. **24**, 19 (2011)
14. de la Fuente, G.F., Navarro, R., Lera, F., Rillo, C., Bartolome, J., Badia, A.: J. Mater. Res. **6**, 699 (1991)
15. Sotelo, A., Madre, M.A., Diez, J.C., Rasekh, Sh., Angurel, L.A., Martinez, E.: Supercond. Sci. Technol. **22**, 034012 (2009)
16. Anderson, P.W., Baskaran, G., Zou, Z., Hsu, T.: Phys. Rev. Lett. **58**, 2790 (1987)
17. Angurel, L.A., de la Fuente, G.F., Badia, A., Larrea, A., Diez, J.C., Pena, J.I., Martinez, E., Navarro, R.: In: Narlikar, A.V. (ed.) Studies of High Temperature Superconductors, vol. 21, p. 1. Nova Science Publishers, New York (1997)
18. Miao, H., Diez, J.C., Angurel, L.A., Pena, J.I., de la Fuente, G.F.: Solid State Ion. **101–103**, 1025 (1997)
19. Bean, C.P.: Phys. Rev. Lett. **8**, 250 (1962)

**Table 1.** $T_c$-onset values of the annealed rods obtained from the data represented in Fig. 6

| | $T_{c\text{-onset}}^{\perp}$ (K) | $T_{c\text{-onset}}^{//}$ (K) |
|---|---|---|
| Pure | 91.5 | 90.7 |
| $X = 0.01$ | 89.4 | 88.2 |
| $X = 0.03$ | 85.2 | 83.3 |
| $X = 0.05$ | 83.5 | 80.6 |
| $X = 0.1$ | 79.9 | 74.6 |

**Figure captions**

**Figure 1.** Powder XRD patterns of pure and Fe-doped annealed textured rods. Increasing doping rate caused the appearance of minor amount of secondary phases. Peaks indicated by ◆ correspond to the Bi-2212 phase

**Figure 2.** Backscattered electron micrographs obtained on longitudinal polished sections of as-grown rods: nominal composition (**a**) $Bi_2Sr_2CaCu_{1.99}Fe_{0.01}O_{8+\delta}$ (**b**) $Bi_2Sr_2CaCu_{1.9}Fe_{0.1}O_{8+\delta}$ (**c**) $Bi_2Sr_2CaCu_{1.9}Fe_{0.1}O_{8+\delta}$ (**d**) dot mapping image of SEM micrograph in (**c**). The representative colors for each element are: Bi: *red*, Sr: *green*, Ca: *blue*, Cu: *light blue*, Fe: *pink*. *Arrows* indicate the Sr, Fe rich 2201 and 2212 intergrowth phases formed after $x = 0.05$ doping level.

**Figure 3.** Backscattered electron micrographs obtained on longitudinal polished sections of annealed thin fibers: nominal composition (**a**) $Bi_2Sr_2CaCu_{1.99}Fe_{0.01}O_{8+\delta}$ (**b**) $Bi_2Sr_2CaCu_{1.9}Fe_{0.1}O_{8+\delta}$ (**c**) $Bi_2Sr_2CaCu_{1.9}Fe_{0.1}O_{8+\delta}$ (**d**) dot mapping image of $Bi_2Sr_2CaCu_{1.9}Fe_{0.1}O_{8+\delta}$ and distribution of all elements on the surface are seen free from each other on small images below. The representative colors for each element are: Bi: *red*, Sr: *green*, Ca: *blue*, Cu: *light blue*, Fe: *pink*. *Arrows* indicate the minor Bi-rich, Ca-poor 2212 phase persists between ideal 2212 phases

**Figure 4.** Magnetization vs. magnetic field curves of Fe-doped annealed rods at 5, 15 and 25 K. Magnetic field was applied both perpendicular (⊥) and parallel (*//*) to the rods growth axis

**Figure 5.** Magnetic field dependence of magnetic critical current densities in the rods, $J_{cm}$, for all the samples at 5, 15, 25 K between 0–9 T

**Figure 6.** Magnetization vs. temperature plots of the annealed rods

**Figure 1**

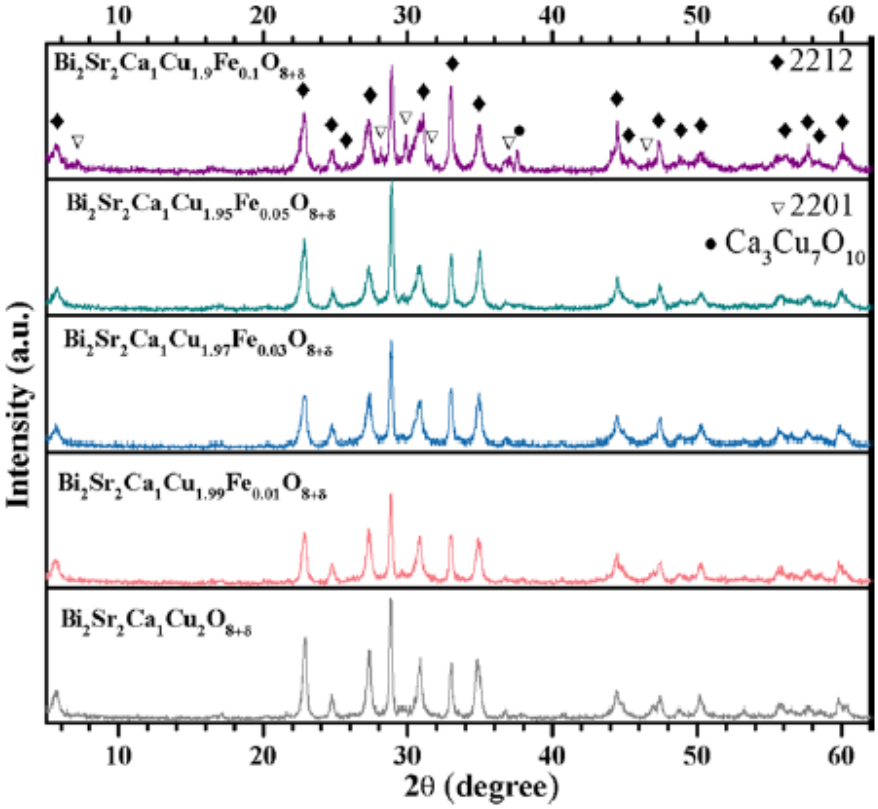
10
20
30
40
50
60
Bi2Sr2Ca1Cu1.9Fe0.1O8+δ
◆2212
Bi2Sr2Ca1Cu1.95Fe0.05O8+δ
▽2201
• Ca3Cu7O10
Bi2Sr2Ca1Cu1.97Fe0.03O8+δ
Bi2Sr2Ca1Cu1.99Fe0.01O8+δ
Bi2Sr2Ca1Cu2O8+δ
Intensity (a.u.)
2θ (degree)

**Figure 2**

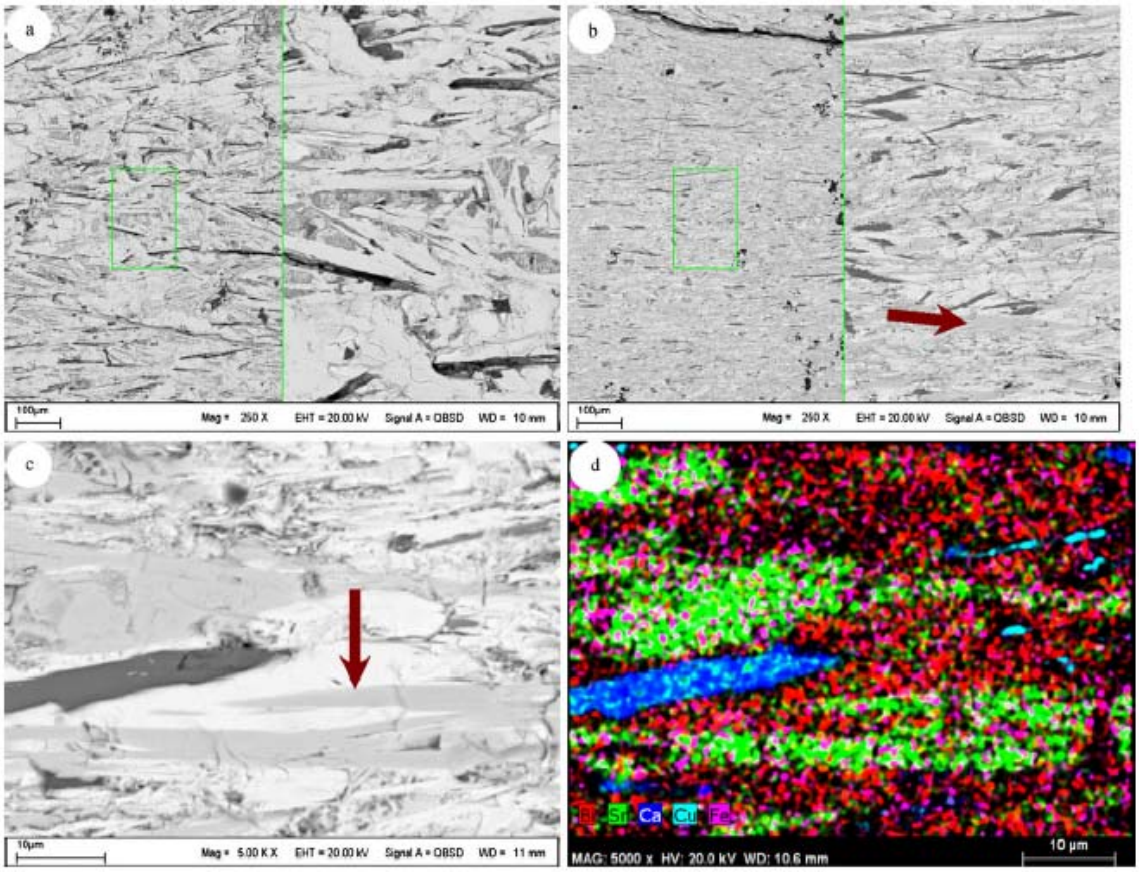
a
100µm
Mag = 250 X EHT = 20.00 kV Signal A = QBSD WD = 10 mm
b
100µm
Mag = 250 X EHT = 20.00 kV Signal A = QBSD WD = 10 mm
c
10µm
Mag = 5.00 K X EHT = 20.00 kV Signal A = QBSD WD = 11 mm
d
Ti Si Ca Cu Fe
MAG: 5000 x HV: 20.0 kV WD: 10.6 mm
10 µm

**Figure 3**

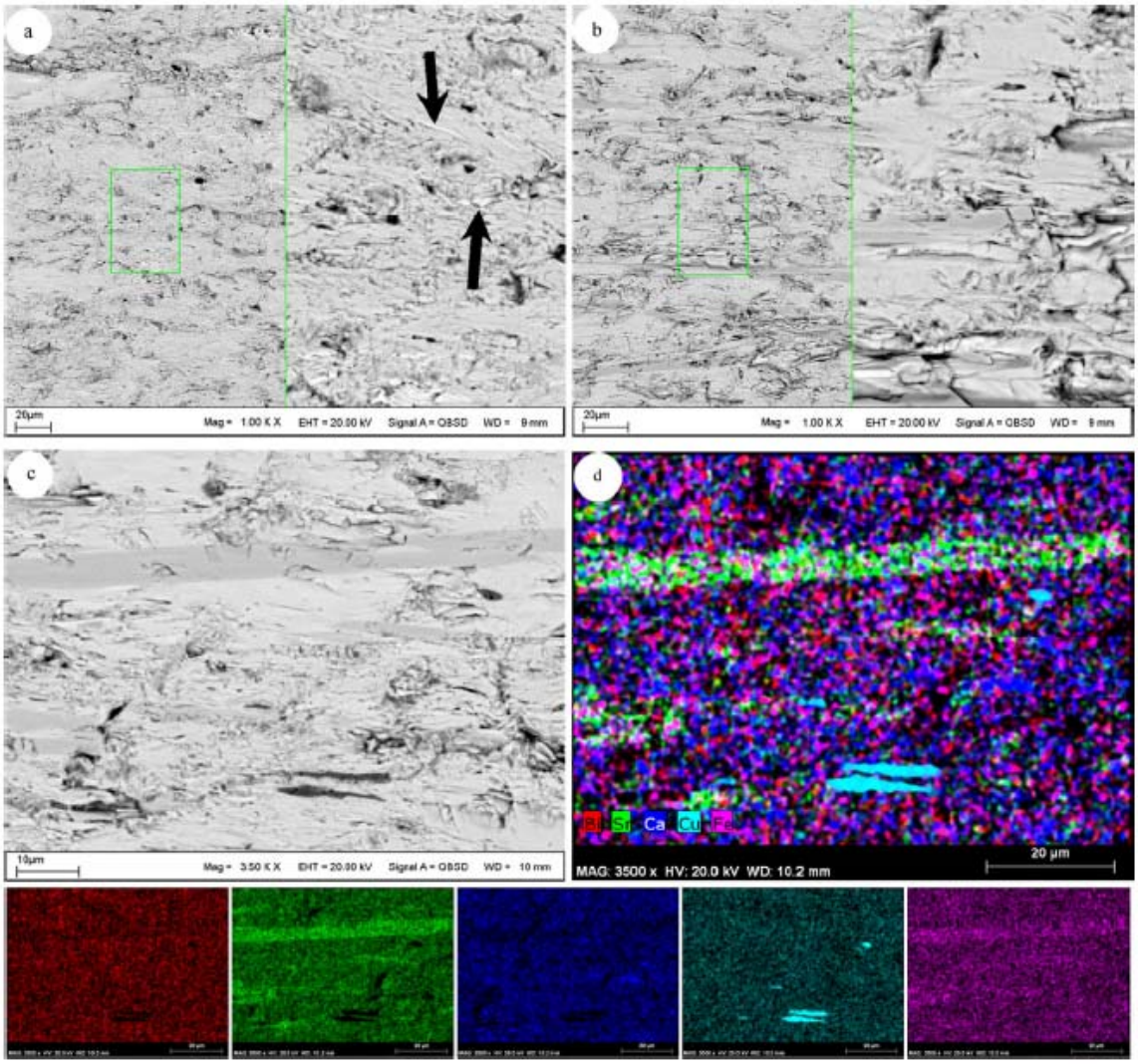
a
20µm
Mag = 1.00 K X EHT = 20.00 kV Signal A = QBSD WD = 9 mm
b
20µm
Mag = 1.00 K X EHT = 20.00 kV Signal A = QBSD WD = 9 mm
c
10µm
Mag = 3.50 K X EHT = 20.00 kV Signal A = QBSD WD = 10 mm
d
Si Ca Cu Fe
20 µm
MAG: 3500 x HV: 20.0 kV WD: 10.2 mm

## Figure 4

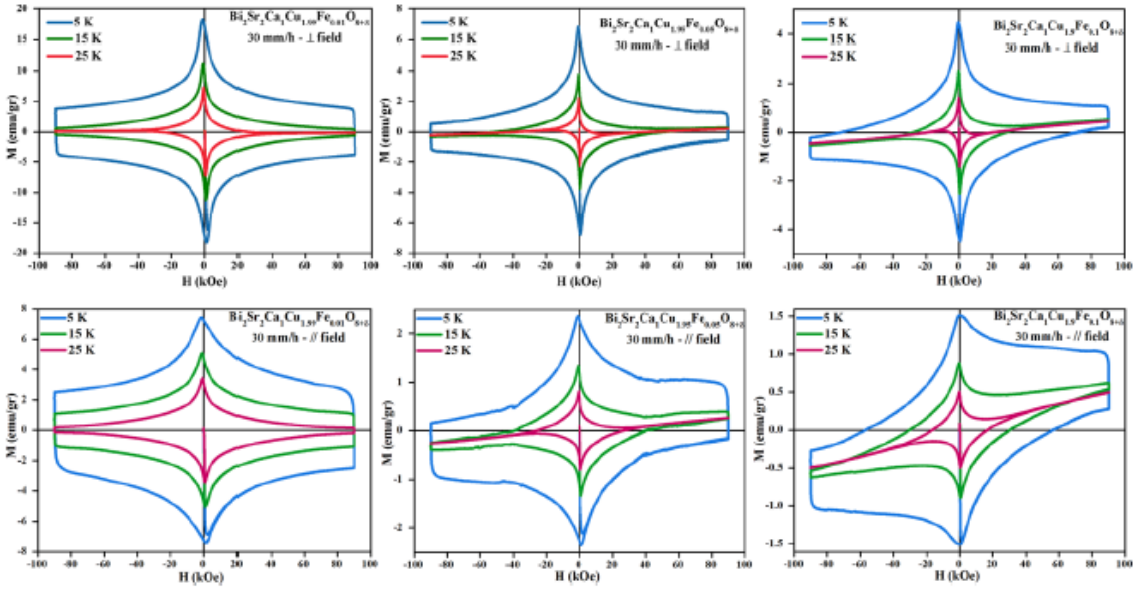

## Figure 5

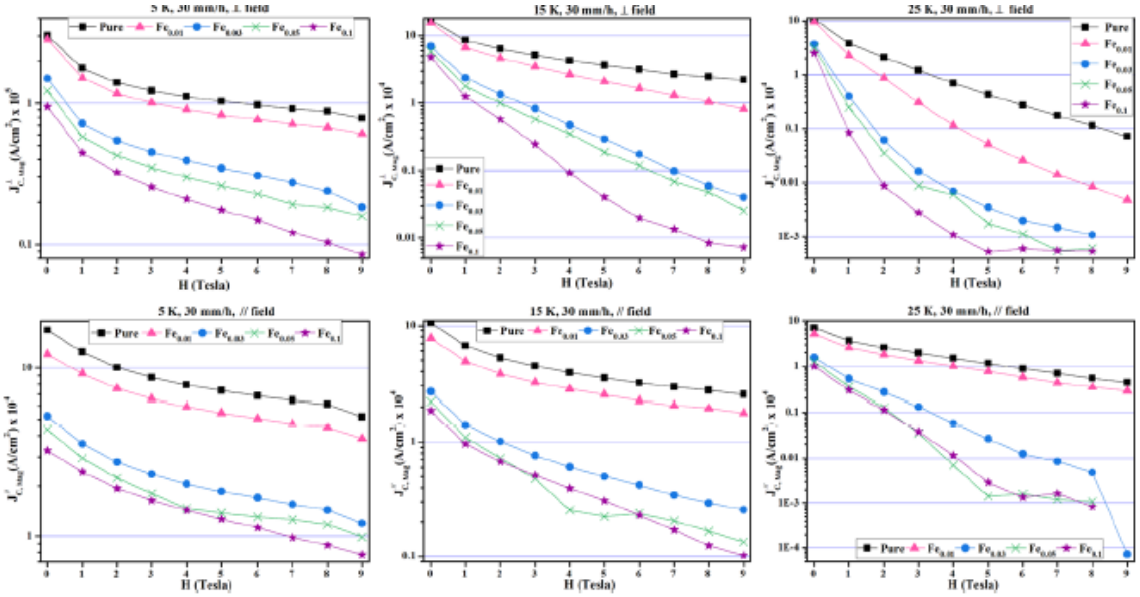
15 K, 30 mm/h, ⊥ field
25 K, 30 mm/h, ⊥ field
5 K, 30 mm/h, // field
15 K, 30 mm/h, // field
25 K, 30 mm/h, // field
Pure
H (Tesla)

**Figure 6**

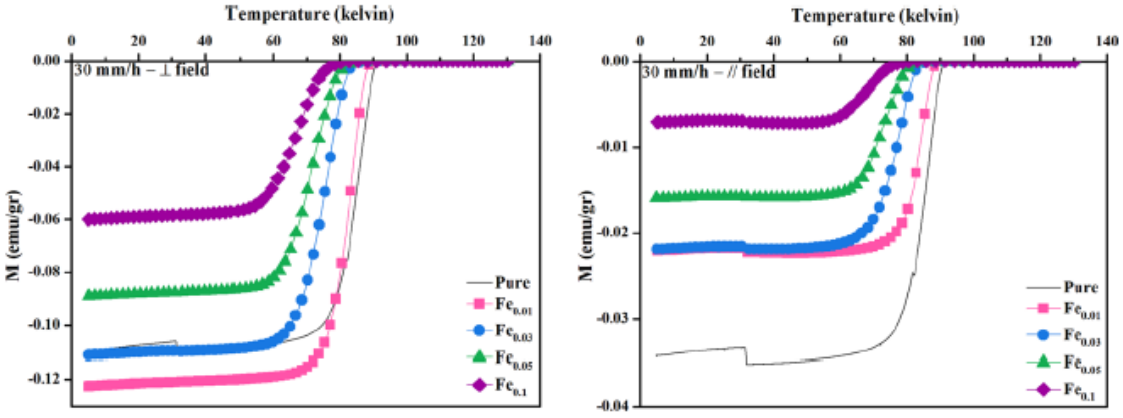
Temperature (kelvin)
30 mm/h – ⊥ field
M (emu/gr)
Pure
Fe0.01
Fe0.03
Fe0.05
Fe0.1
Temperature (kelvin)
30 mm/h – // field
M (emu/gr)
Pure
Fe0.01
Fe0.03
Fe0.05
Fe0.1